UV Exoplanet Transmission Spectral Features as Probes of Metals and Rainout

Joshua D. Lothringer[1] , Guangwei Fu[2] , David K. Sing[1,3] , and Travis S. Barman[4]
[1] Department of Physics and Astronomy, Johns Hopkins University, Baltimore, MD, USA; jlothri1@jhu.edu
[2] Department of Astronomy, University of Maryland, College Park, MD, USA
[3] Department of Earth & Planetary Sciences, Johns Hopkins University, Baltimore, MD, USA
[4] Lunar and Planetary Laboratory, University of Arizona, Tucson, AZ, USA

Abstract

The transmission spectra of ultra-hot Jupiters observed shortward of 0.5 μm indicate strong absorption. Previous explanations have included scattering, photochemistry, escaping metals, and disequilibrium chemistry. In this Letter, we show that slopes and features shortward of 0.5 μm can be caused by opacity not commonly considered in atmosphere models of exoplanets but guaranteed to be present if conditions are near chemical equilibrium including, but not limited to, atoms and ions of Fe, Ti, Ni, Ca, Cr, Mn, and SiO. Using the PHOENIX atmosphere model, we describe how the short-wavelength transit spectrum varies with equilibrium temperature between 1000 K and 4000 K, as well as the effect that the rainout of condensates has at these wavelengths. We define two spectral indices to quantify the strength of the NUV and blue absorption compared to that in the red-optical, finding that the NUV transit depth will significantly exceed the transit depth from Rayleigh scattering alone for all hot Jupiters down to around 1000 K. In the blue-optical, hot Jupiters warmer than 2000 K will have transit depths larger than that from Rayleigh scattering, but below 2000 K, Rayleigh scattering can dominate, if present. We further show that these spectral indices may be used to trace the effects of rainout. We then compare our simulated transit spectra to existing observations of WASP-12b, WASP-33b, WASP-76b, and WASP-121b. Further observation of exoplanets at these wavelengths should be prioritized in the coming years as the Hubble Space Telescope nears the end of its operational capability.

1. Introduction

The spectral footprint of different atmospheric components can be identified through transmission spectroscopy. Light from the host star is effectively filtered through a planet's terminator, allowing us to identify and characterize the composition and, to a lesser degree, the temperature of the atmosphere.

By combining Hubble Space Telescope (HST)/STIS and WFC3 grisms, complete low-resolution transit spectra between 0.3 and 1.7 μm have been obtained for several planets to date (e.g., Sing et al. 2016). In this range, one usually seeks to detect and characterize molecular absorption from H_2O, TiO, and VO, as well as broad alkali lines from Na and K. Aerosol opacity, from either condensate clouds or photochemical hazes, can be inferred by detecting a uniform gray opacity or scattering slopes toward short wavelengths.

Large transit depths at short wavelengths have been found in a number of exoplanets (e.g., Ballester et al. 2007; Lecavelier Des Etangs et al. 2008; Pont et al. 2008; Sing et al. 2008) and have frequently been well-fit by scattering, often approximated by

$$\sigma = \sigma_0 (\lambda/\lambda_0)^{-\alpha}, \qquad (1)$$

where λ is the wavelength, λ_0 is the reference wavelength, σ is the scattering cross-section, σ_0 is the cross-section at the reference wavelength, and $\alpha = 4$ in the case of Rayleigh scattering. Unocculted starspots can also cause increased short-wavelength transit depths (Pont et al. 2013; McCullough et al. 2014; Rackham et al. 2018).

Recent observational and theoretical studies into the hottest known Jovian exoplanets, called ultra-hot Jupiters, have shown a plethora of atomic species and their ions can exist in these planets' atmospheres (e.g., Arcangeli et al. 2018; Kitzmann et al. 2018; Lothringer et al. 2018; Parmentier et al. 2018; Yan & Henning 2018; Casasayas-Barris et al. 2019; Hoeijmakers et al. 2019; Lothringer & Barman 2019). At equilibrium temperatures of more than 2000 K, molecules begin to thermally dissociate, atoms ionize, and condensation of even the most refractory elements ceases. The effect of these atomic species on short-wavelength exoplanet transmission spectra has yet to be fully explored.

Indeed, transmission spectra of ultra-hot Jupiters WASP-12b, WASP-33b, WASP-76b, and WASP-121b all show significant absorption at wavelengths less than 0.5 μm. The moderate slope in the optical transmission spectrum of WASP-12b has thus far been interpreted as being caused by scattering by hazes (Sing et al. 2013; Kreidberg et al. 2015), while the NUV spectrum from HST/COS shows evidence of escaping metals (Fossati et al. 2010; Haswell et al. 2012). The short-wavelength absorption in WASP-33b was interpreted as being from AlO, which would be highly out of equilibrium, but could explain absorption between 0.4 and 0.5 μm (von Essen et al. 2019). The slope in WASP-121b was interpreted as being from the photochemical product SH (Evans et al. 2018, see also Zahnle et al. 2009), though additional observations with Swift/UVOT and HST/STIS/E230M show that this slope continues below 0.3 μm with evidence of escaping Fe II and Mg II (Salz et al. 2019; Sing et al. 2019). Fe I has also been detected in WASP-121b in multiple data sets (Bourrier et al. 2020; Cabot et al. 2020; Gibson et al. 2020).
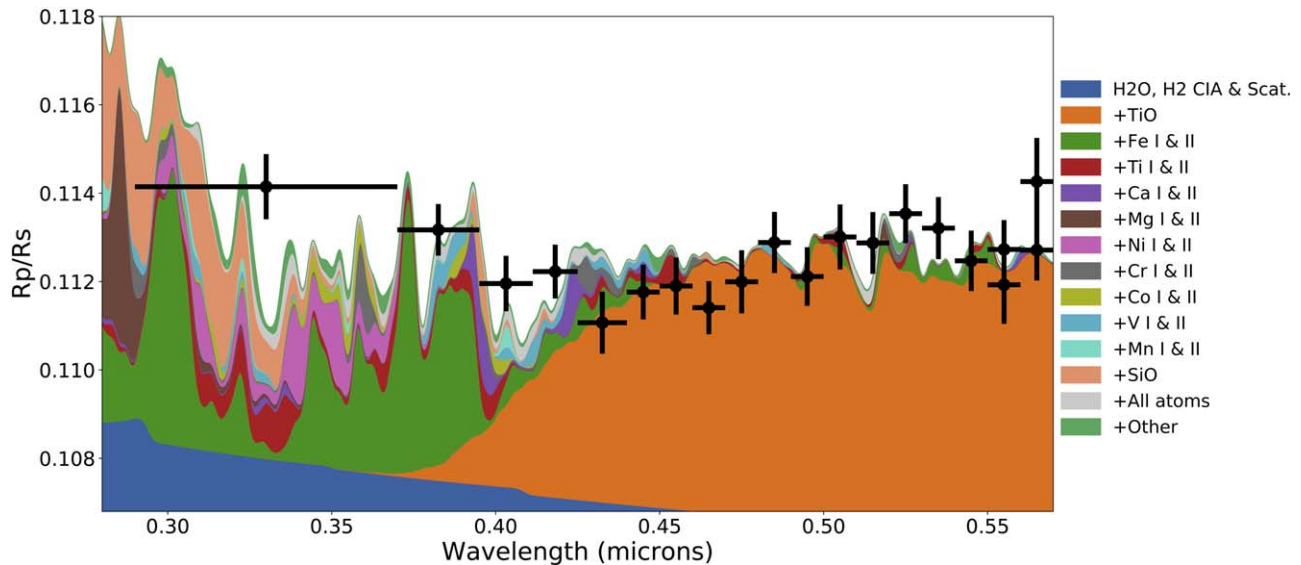
Figure 1. Contribution of various opacity sources sequentially added to the transit spectrum of WASP-76b.

The recent transmission spectrum of WASP-76b ($T_{\rm eq} = 2160$ K) also shows large NUV and blue transit depths in addition to TiO and H_2O opacity (Fu et al. 2020). These observations were well-fit by a self-consistent atmosphere model at solar metallicity, without the need to appeal to disequilibrium processes. It was shown that the large transit depths at short wavelengths can be caused by opacity not commonly considered in atmosphere models of exoplanets, but guaranteed to be present in chemical equilibrium including Fe and SiO. The presence of Fe I in WASP-76b has also been detected with ground-based high-resolution observations, with evidence that it is gaseous on the evening terminator, but condenses on the nightside (Ehrenreich et al. 2020).

In this Letter, we study these important opacity sources further by computing additional hot Jupiter short-wavelength transmission spectra. In Section 2, we describe our modeling setup. In Section 3, we discuss our model spectrum of WASP-76b, explore how the short-wavelength transit spectrum varies with temperature, investigate atmospheric heating by NUV opacity sources, and compare our models to observations of other ultra-hot Jupiters. In Section 4, we close with further discussion and conclusions.

2. Methods

We use the PHOENIX atmosphere model to calculate the composition, structure, opacity, and transmission spectrum of several hot Jupiters. Our model setup is similar to previous studies of ultra-hot Jupiters (Lothringer et al. 2018; Lothringer & Barman 2019). PHOENIX self-consistently calculates the composition and structure of an atmosphere assuming chemical and radiative-convective equilibrium, including the irradiation from a primary companion (Hauschildt et al. 1999; Barman et al. 2001). We consider some models with rainout chemistry, where an element will be depleted in layers above if it is present in condensates in the lower atmosphere. Our rainout models assume efficient settling and no vertical mixing and thus represent the limiting behavior of rainout.

Thanks to its large EUV-to-FIR opacity database of atomic opacity up to uranium (e.g., Kurucz 1994) and over 130 molecular species, PHOENIX is ideal to model ultra-hot

exoplanets, particularly at short wavelengths. While PHOENIX includes a vast array of opacity data (some retained for historical or special purposes), our models contain the minimum number of restrictions on the opacities we use, resulting in the most complete set of opacity sources currently available to us. Our comprehensive investigation allows us to remain agnostic about which species are the most important opacity sources. The dominant molecular opacity in our model are from SiO (Kurucz 1993), TiO (Schwenke 1998), and H_2O (Barber et al. 2006).

3. Results and Discussion

3.1. WASP-76b

Fu et al. (2020) present a transit spectrum of WASP-76b ($T_{\rm eq} = 2180$ K) from 0.3–5 μm using data from HST/STIS/ G430L, HST/STIS/G750L, HST/WFC3/G141, and Spitzer channels 1 and 2. The retrievals in Fu et al. (2020) using PLATON ($\chi_\nu^2 = 2.28$; Zhang et al. 2019) and ATMO ($\chi_\nu^2 = 1.94$; Amundsen et al. 2014; Evans et al. 2017) require either an unphysically strong scattering slope or a high Fe abundance, respectively, to fit the short-wavelength slope; however, the spectrum is also well-fit by a self-consistent cloud-free chemical-equilibrium solar-metallicity PHOENIX model ($\chi_\nu^2 = 2.66$). TiO and H_2O are evident in the spectra as strong absorption between 0.45 and 1.0 μm and 1.3–1.6 μm, respectively. Fe alone does not provide enough opacity to fit the slope toward increasing transit depth with decreasing wavelength shortward of 0.45 μm. Additional opacity from a number of metals and molecules contribute to fit the observations, including Ti I, Ni I, Ca I & II, and SiO.

Figure 1 shows the contribution of these various atoms and molecules sequentially added to the transit spectrum of WASP-76b compared to the data. As opacity from TiO begins to drop off shortward of 0.45 μm, Fe opacity begins to increase. Strong lines from Ca and Cr add to a bump at 0.43 μm. This region, between 0.43 and 0.5 μm, does not agree well with the data, possibly indicating some of these species may not be present in the gas phase or are otherwise weaker than our model predicts. The Ca II H and K lines are evident at 0.39 μm with additional
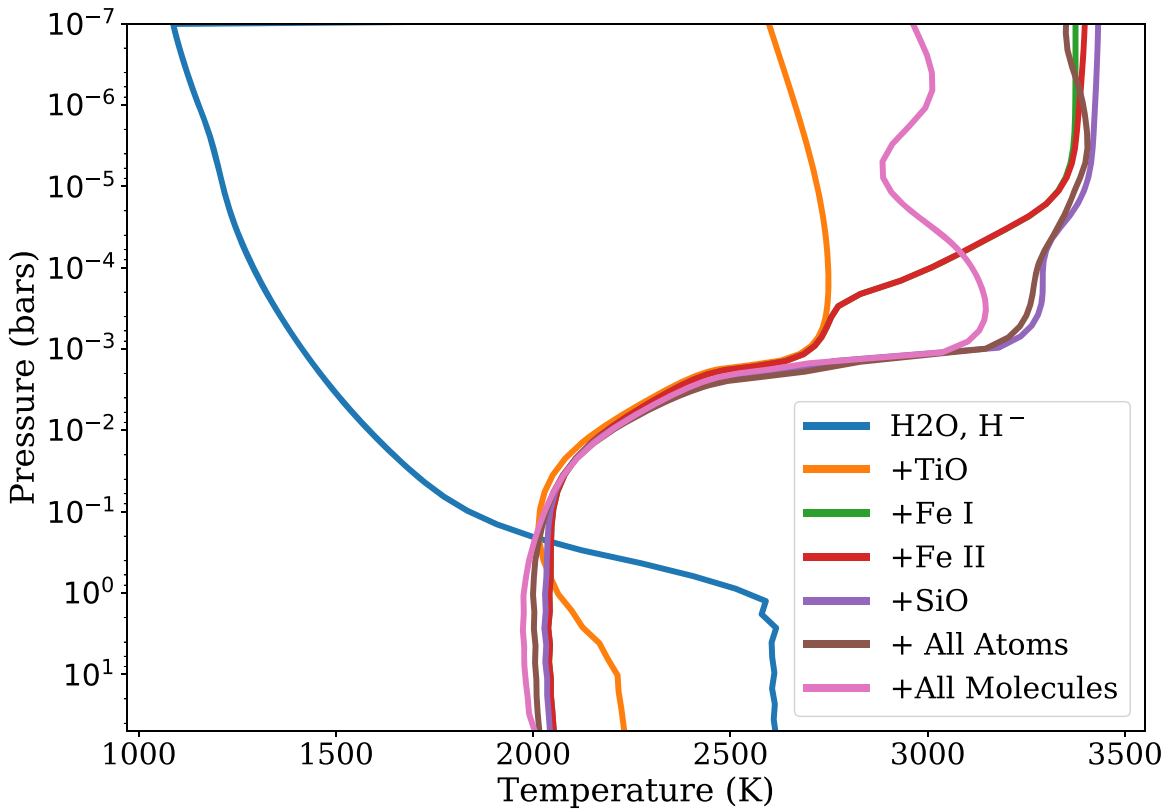
Figure 2. Temperature structures from models of WASP-76b sequentially adding different opacity sources. "All Atoms" includes atomic opacity up to uranium and "All Molecules" refers to all 130 molecular species available in our version of PHOENIX.

opacity from V I and a band of Fe I lines between 0.37 and 0.39 μm. Strong Fe I and Cr I lines at 0.36 μm produce another bump in transit depth. Ni I and II provide a forest of lines between 0.34 and 0.36 μm. SiO becomes a major opacity source shortward of 0.35 μm and helps explain the shortest-wavelength bin of the HST/STIS observations when combined with a major Fe I band at 0.3 μm. While shortward of the current WASP-76b HST/STIS data, the Mg II doublet has been observed well past the planetary Roche lobe in WASP-12b (Fossati et al. 2010) and WASP-121b (Sing et al. 2019), but not in the much cooler HD 209458b (Cubillos et al. 2020). VO can also provide significant opacity in the right conditions. Evans et al. (2018) suggest that the transmission spectrum of ultra-hot Jupiter WASP-121b can be explained by TiO condensing out of the atmosphere, leaving VO as the main opacity between 0.45 and 1.1 micron. In the scenario presented in Figure 1, TiO remains about 50 times more abundant in equilibrium, covering up most of the contribution from VO. VO thus only plays a very minor role, slightly increasing the opacity longward of 0.7 microns. The contribution from all other opacity sources, from atoms like Cu to molecules like MgH, only have a very minor effect on the short-wavelength transit spectrum in chemical equilibrium.

Figure 2 shows the converged temperature structure of several models sequentially including different sets of UV opacity sources in order to examine their contribution to atmosphere heating. The large temperature inversion in ultra-hot Jupiters is caused by heating from the absorption of NUV and optical irradiation by atoms and molecules like TiO, Fe I & II, and SiO (Hubeny et al. 2003; Fortney et al. 2008; Lothringer et al. 2018; Gandhi & Madhusudhan 2019). This level of

atmospheric heating has also been suggested in the context of WASP-121b's UV absorber (Evans et al. 2018). The inclusion of all molecular opacities results in some cooling of the upper atmosphere due to radiative cooling in the infrared by CO. While outside the scope of this Letter, the detailed influence of trace metals on the energy balance in the upper atmosphere is worth future investigation.

3.2. Generic Hot Jupiter

To explore how the short-wavelength transit spectrum varies with temperature, we calculated atmosphere models for a generic hot Jupiter at several equilibrium temperatures: 770, 1100, 1290, 1580, 1890, 2250, 2680, 3184, and 4500 K, corresponding to 8×, 4×, 3×, 2×, 1.4×, 1×, 0.7×, 0.5×, and 0.25× the orbital distance of the 2250 K model, respectively. The properties of the generic hot Jupiter are identical to those used in Lothringer et al. (2018) and Lothringer & Barman (2019), namely 1 M_J and 1.5 R_J orbiting a 1.5 R_{Sun} 7200 K F0 star. Figure 3 shows a subset of these, including the 770, 1290, 1580, 2250, 2677, and 3184 K models. We also ran models with the same temperature structure, but with rainout included in the chemistry, indicated by dashed lines in Figure 3.

Overall, the short-wavelength transit slope decreases in magnitude with decreasing temperature as metals and other species condense out of the gas phase. This is further enhanced in the rainout models where an element will be depleted in the upper atmosphere if it condenses in the lower atmosphere. The effect of rainout on the NUV and blue-optical opacities was previously pointed out in the context of HD 209458b in Barman (2007). At red wavelengths, TiO and VO begin to rain out of the atmosphere around 2000 K, revealing the strong
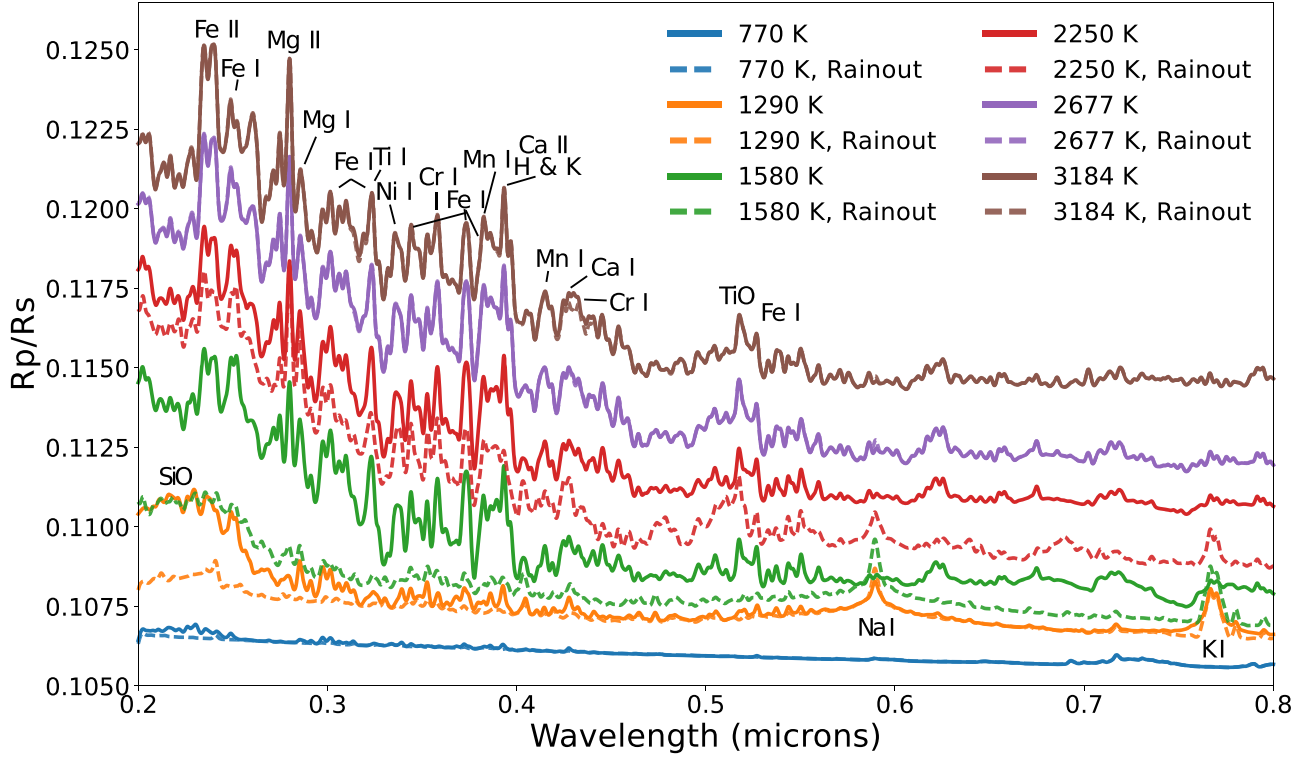
Figure 3. Transit spectra between 0.2 and 0.8 μm of the fiducial generic hot Jupiter at different temperatures. Solid lines indicate local chemical equilibrium, while dashed lines indicate models with rainout chemistry. For the 2677 K and 3184 K models, no condensation takes place so the dashed line is identical to the solid line. Only a small offset has been applied to the 1580 K chemical-equilibrium model for clarity, otherwise their spacing is the natural effect of their different scale heights as each model has the same radius at the bottom of the model (i.e., 1.5 R_J at $\tau_{1.2\mu\text{m}} = 1000$).

pressure-broadened Na and K resonance line wings, which themselves condense around 1000 K. Above 2000 K, the Na and K line cores can still be detected at high-resolution as in Seidel et al. (2019).

3.2.1. Spectral Indices

We quantify the strength of the short-wavelength opacity by defining two spectral indices. The first, $\Delta R_{p,\text{NUV}-\text{Red}}$, compares the transit radius of the planet between 0.2 and 0.3 μm with the radius between 0.6 and 0.7 μm. The indices are normalized by the atmospheric scale height at the equilibrium temperature (H = $kT_{\text{eq}}/\mu g$) such that a dimensionless quantity can be compared across planets with varying gravity and temperatures. Differences in the surface gravity and temperature structure on planets at the same equilibrium temperature can still result in changes up to about 10% in these indices. We also note that the NUV spectrum between 0.2 and 0.3 μm may probe high enough in the atmosphere to be dominated by escaping gas (e.g., Fossati et al. 2010; Vidal-Madjar et al. 2013; Sing et al. 2019), so the transit depths that we calculate in that range are likely a lower limit. The second spectral index, $\Delta R_{p,\text{Blue}-\text{Red}}$, compares the transit radius of the planet between 0.3 and 0.4 μm (approximately the bluest bin in G430L observations) with the radius between 0.6 and 0.7 μm. Formally,

$$\Delta R_{p,\text{NUV}-\text{Red}} = \frac{R_{p,0.2-0.3\mu\text{m}} - R_{p,0.6-0.7\mu\text{m}}}{H_{\text{eq}}} \quad (2)$$

and

$$\Delta R_{p,\text{Blue}-\text{Red}} = \frac{R_{p,0.3-0.4\mu\text{m}} - R_{p,0.6-0.7\mu\text{m}}}{H_{\text{eq}}}. \quad (3)$$

We plot these two indices as a function of equilibrium temperature in Figure 4 using the models described in Section 3.2. $\Delta R_{p,\text{NUV}-\text{Red}}$ remains high for all temperatures, and, in particular, is above the slope expected from Rayleigh scattering alone, assuming opacity of the form $\sigma = \sigma_0(\lambda/\lambda_0)^{-4}$, for all scenarios except the coldest rainout models. Up to 9 scale heights are probed across the spectral index, implying the spectral imprint of the opacity sources we discuss here should be readily observable for a wide range of systems.

At high temperatures, models with chemical equilibrium are similar to those with rainout chemistry; however, $\Delta R_{p,\text{NUV}-\text{Red}}$ begins to decrease more steeply for models with rainout compared to those in chemical equilibrium. This is expected, as opacity sources that absorb strongly in the NUV will be depleted in the atmosphere at higher temperatures compared to chemical equilibrium if they rainout once condensation starts lower in the atmosphere. $\Delta R_{p,\text{NUV}-\text{Red}}$ is greater in the rainout models than in chemical equilibrium for the T = 1887 and 2677 K models because TiO and VO also begin to rainout of the atmosphere at this temperature, decreasing the transit radius between 0.6 and 0.7 μm, subsequently raising $\Delta R_{p,\text{NUV}-\text{Red}}$. $\Delta R_{p,\text{NUV}-\text{Red}}$ gradually decreases above 2677 K as H$^-$ opacity begins to raise the transit depths at red and IR wavelengths.

The behavior of $\Delta R_{p,\text{Blue}-\text{Red}}$ is somewhat more complicated. At 2000 K, there is a turnover from the index being dominated by Rayleigh scattering to being dominated by the
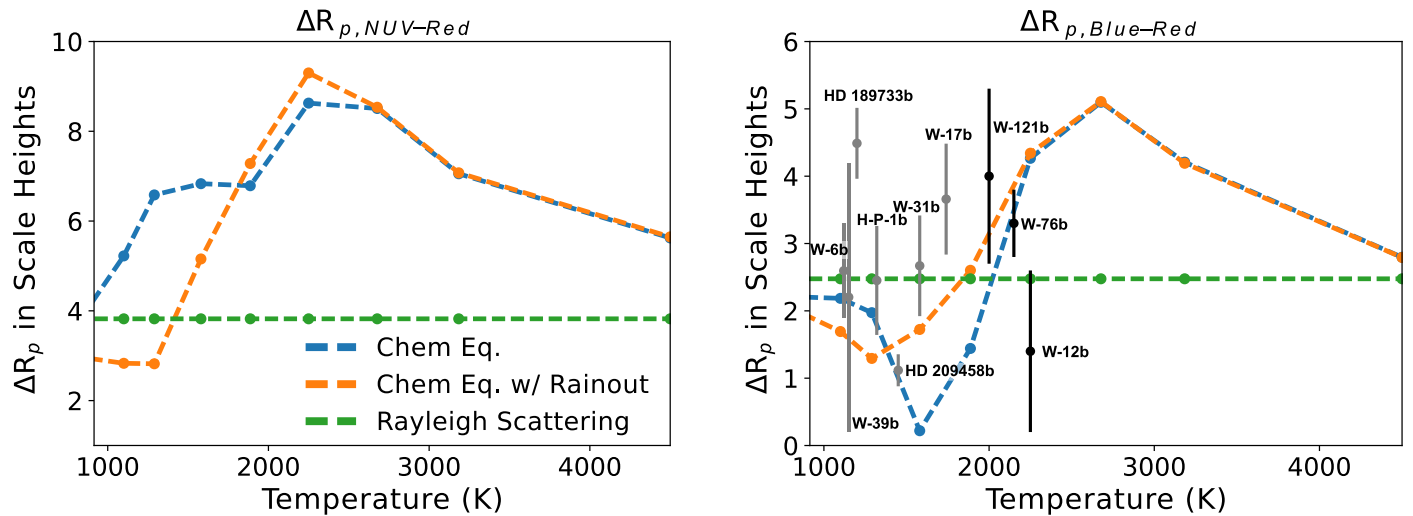
Figure 4. Left: the $\Delta R_{p,\mathrm{NUV-Red}}$ spectral index, quantifying the difference between the transit radius, in terms of scale heights, between 0.2–0.3 μm and 0.6–0.7 μm as a function of temperature. Right: same as left, but for the $\Delta R_{p,\mathrm{Blue-Red}}$, measured between 0.3–0.4 μm and 0.6–0.7 μm. Also plotted is the expected slope from Rayleigh scattering.

gas opacities. For planets above 2000 K, we expect the gas opacities we describe here to result in a larger $\Delta R_{p,\mathrm{Blue-Red}}$ than from Rayleigh scattering alone. Below 2000 K; however, we expect the blue transit depths caused by Rayleigh scattering to be larger than that caused by gas opacity.

3.3. Comparison to Previous Observations

Only three hot Jupiters have reported observations between 0.2 and 0.3 μm: WASP-12b (Fossati et al. 2010), HD 209458b (Vidal-Madjar et al. 2013), and WASP-121b (Sing et al. 2019). WASP-12b and WASP-121b have $\Delta R_{p,\mathrm{NUV-Red}}$ values of 66 and 25 planetary scale heights, respectively, far above our model predictions. These wavelengths trace escaping (i.e., nonhydrostatic) gas, a process not accounted for in our hydrostatic models. For HD 209458b, however, Vidal-Madjar et al. (2013) and Cubillos et al. (2020) both find the observations consistent with Rayleigh scattering, but not precise enough to constrain its slope. Additional observations of these and other targets at short wavelengths, can constrain the behavior of the atmosphere (e.g., escaping versus hydrostatic), the metal content of hot Jupiter middle and upper atmospheres, and the effects of rainout chemistry as a function of planetary parameters.

Overplotted on Figure 4 are the indices for a number of hot Jupiters from Sing et al. (2016) for which short-wavelength and NIR transit observations exist, allowing us to approximate the value of $\Delta R_{p,\mathrm{Blue-Red}}$. These planets are plotted at their equilibrium temperatures. Interestingly, HD 209458b, whose optical spectrum is well-fit by our rainout model, is the only planet >2σ below the maximum $\Delta R_{p,\mathrm{Blue-Red}}$ suggested by Figure 4.

Also shown in Figure 4 are the indices for the ultra-hot Jupiters WASP-12b, WASP-76b, and WASP-121b, whose full spectra are also shown in Figure 5. These three hottest planets are each plotted at their best-fit terminator temperature, which is cooler than the planets' equilibrium temperature for WASP-12b and WASP-121b. For WASP-76b and WASP-121b, scattering is not indicated by the rest of their respective transit spectra and the short-wavelength in particular is well fit by our cloud- and haze-free models. Scattering by aerosols was,

however, the original interpretation of the WASP-12b observations in Sing et al. (2013). While we cannot rule out scattering, the additional short-wavelength opacity discussed here provides a qualitatively similar fit with $\chi^2_\nu = 2.15$.

Our self-consistent models for these three planets have suitable fits, despite having no free parameters besides a small DC offset in R_p/R_s to best match the observations and a rough fit in temperature . For each planet, we calculate models assuming full, dayside, and no heat redistribution and then find the best fitting spectrum. While the goodness-of-fit for most of the self-consistent models is comparable to that of the retrieved models for WASP-76b (Fu et al. 2020), adjusting additional parameters like metallicity or the temperature profile would likely improve the fit to each of the data sets.

This is especially true for WASP-121b, for which previous analyses prefer increased metallicity, no TiO, and a low temperature (compared to its equilibrium temperature; Mikal-Evans et al. 2019; Hoeijmakers et al. 2020). Informed by these previous results, we include a model cooler than full redistribution by 300 K, as well as a model with no TiO. With TiO, our best fit has $\chi^2_\nu = 6.9$, while without TiO, we obtain $\chi^2_\nu = 2.37$.

In Figure 5, we also plot transit spectrum of WASP-33b from 0.4 to 0.9 μm. The spectrum stands out as qualitatively poorly fit by our self-consistent models , though the fit does have a reasonable χ^2_ν of 1.78. Taken over the course of two nights at Gran Telescopio Canarias, these observations were originally interpreted as an indication of AlO opacity between 0.4 and 0.5 μm (von Essen et al. 2019). AlO would have to be highly out of equilibrium to explain the observed spectrum, as Al is preferentially in AlH or its atomic form at these temperatures. We suggest further observations at these wavelengths for this valuable system to confirm the behavior of WASP-33b's short-wavelength transit spectrum.

4. Conclusions

Inspired by the recent transit spectrum of ultra-hot Jupiter WASP-76b (Fu et al. 2020), we have modeled the short-wavelength transit spectrum of hot Jupiters. We show that large transit depths, especially for ultra-hot Jupiters, can be expected
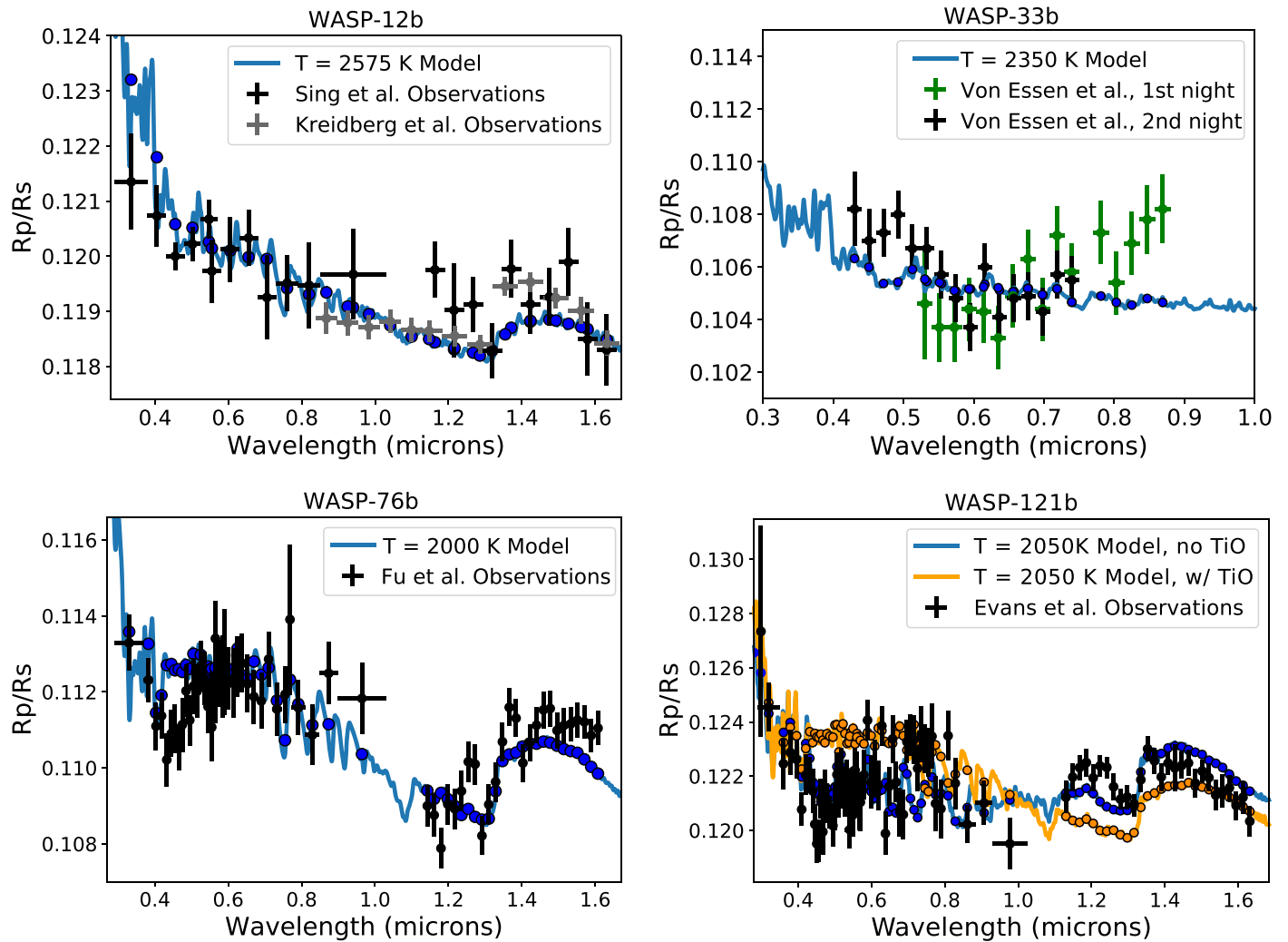
Figure 5. Observed transit spectra of four ultra-hot Jupiters with wavelength coverage below 0.5 μm compared to self-consistent models.

at NUV and blue wavelengths due to opacity from many species not considered at longer wavelengths, like Fe, Ti, Ni, V, Cr, and SiO. We emphasize that all the species discussed here are guaranteed to be present if conditions in the atmosphere are near chemical equilibrium and only efficient disequilibrium mechanisms, like cold-trapping and rainout, could preclude their imprint on short-wavelength transit spectra. After submission of this work, some of the species we discussed here, namely V and Cr were detected in WASP-121b in high-resolution ground-based spectra (Ben-Yami et al. 2020; Hoeijmakers et al. 2020).

We defined two spectral indices to quantify the magnitude of the UV and blue-wavelength transit depths compared to red-wavelength transit depths as a function of temperature. We showed that the transit depth between 0.2 and 0.3 μm is always larger than would be expected for Rayleigh scattering alone, except for in the coldest cases considered with rainout chemistry. At slightly longer wavelengths, between 0.3 and 0.4 μm, there is a turnover compared to Rayleigh scattering at 2000 K, where Rayleigh scattering can dominate at lower temperatures, while gas opacity will dominate at higher temperatures. The relationship between these indices and temperature changes if rainout chemistry is considered, providing a future path to characterizing processes occurring in the deeper atmosphere.

We recommend future observations at these wavelengths to identify the presence or absence of species. From space, this will require the use of HST/STIS or HST/WFC3/UVIS/G280, the latter of which shows great promise at characterizing the entire NUV-optical transit spectrum (Wakeford et al. 2020) and could simultaneously measure the three spectral indices we have defined. Low-resolution, short-wavelength HST transit spectra would not only be able to detect opacity from metals, but would also be capable of detecting the effects of rainout if a variety of hot Jupiter targets are observed. Additionally, the Colorado Ultraviolet Transit Experiment (CUTE), slated to launch in 2020, will characterize the 2550–3300 Å transmission spectrum of several hot and ultra-hot Jupiters at medium spectral-resolution with a 6-unit CubeSat (Fleming et al. 2017). By combining several transits together, CUTE has the potential to detect species like Mg I and II at SNR~10–100. With HST/STIS/E230M and from the ground, high-resolution spectroscopy have already found success detecting and characterizing a plethora of species in the optical spectra of ultra-hot Jupiters (e.g., Hoeijmakers et al. 2019; Sing et al. 2019; Ehrenreich et al. 2020; Gibson et al. 2020). With more observations, trends between the presence and abundance of these species with planetary properties like equilibrium temperature, like those suggested in Figures 3 and 4, can be identified.

ORCID iDs

Joshua D. Lothringer ⓘ https://orcid.org/0000-0003-3667-8633
Guangwei Fu ⓘ https://orcid.org/0000-0002-3263-2251
David K. Sing ⓘ https://orcid.org/0000-0001-6050-7645
Travis S. Barman ⓘ https://orcid.org/0000-0002-7129-3002

References

Amundsen, D. S., Baraffe, I., Tremblin, P., et al. 2014, A&A, 564, A59
Arcangeli, J., Désert, J.-M., Line, M. R., et al. 2018, ApJ, 855, L30
Ballester, G. E., Sing, D. K., & Herbert, F. 2007, Natur, 445, 511
Barber, R. J., Tennyson, J., Harris, G. J., & Tolchenov, R. N. 2006, MNRAS, 368, 1087
Barman, T. 2007, ApJL, 661, L191
Barman, T. S., Hauschildt, P. H., & Allard, F. 2001, ApJ, 556, 885
Ben-Yami, M., Madhusudhan, N., Cabot, S. H. C., et al. 2020, ApJ, 897, 5
Bourrier, V., Ehrenreich, D., Lendl, M., et al. 2020, A&A, 635, 205
Cabot, S. H. C., Madhusudhan, N., Welbanks, L., Piette, A., & Gandhi, S. 2020, MNRAS, 494, 363
Casasayas-Barris, N., Pallé, E., Yan, F., et al. 2019, A&A, 628, A9
Cubillos, P. E., Fossati, L., Koskinen, T., et al. 2020, AJ, 159, 111
Ehrenreich, D., Lovis, C., Allart, R., et al. 2020, Natur, 580, 597
Evans, T. M., Sing, D. K., Goyal, J. M., et al. 2018, AJ, 156, 283
Evans, T. M., Sing, D. K., Kataria, T., et al. 2017, Natur, 548, 58
Fleming, B. T., France, K., Nell, N., et al. 2017, Proc. SPIE, 10397, 103971A
Fortney, J. J., Lodders, K., Marley, M. S., & Freedman, R. S. 2008, ApJ, 678, 1419
Fossati, L., Haswell, C. A., Froning, C. S., et al. 2010, ApJL, 714, L222
Fu, G., Deming, D., Lothringer, J., et al. 2020, arXiv:2005.02568

Gandhi, S., & Madhusudhan, N. 2019, MNRAS, 485, 5817
Gibson, N. P., Merritt, S., Nugroho, S. K., et al. 2020, MNRAS, 493, 2215
Haswell, C. A., Fossati, L., Ayres, T., et al. 2012, ApJ, 760, 79
Hauschildt, P. H., Allard, F., & Baron, E. 1999, ApJ, 512, 377
Hoeijmakers, H. J., Ehrenreich, D., Kitzmann, D., et al. 2019, A&A, 627, A165
Hoeijmakers, H. J., Seidel, J. V., Pino, L., et al. 2020, A&A, in press (arXiv:2006.11308)
Hubeny, I., Burrows, A., & Sudarsky, D. 2003, ApJ, 594, 1011
Hunter, J. D. 2007, CSE, 9, 90
Kitzmann, D., Heng, K., Rimmer, P. B., et al. 2018, ApJ, 863, 183
Kreidberg, L., Line, M. R., Bean, J. L., et al. 2015, ApJ, 814, 66
Kurucz, R. 1993, Diatomic Molecular Data for Opacity Calculations, Kurucz CD-ROM No. 15 (Cambridge, MA: Smithsonian Astrophysical Observatory)
Kurucz, R. 1994, Atomic Data for Fe and Ni, Kurucz CD-ROM No. 22 (Cambridge, MA: Smithsonian Astrophysical Observatory)
Lecavelier Des Etangs, A., Pont, F., Vidal-Madjar, A., & Sing, D. 2008, A&A, 481, L83
Lothringer, J. D., & Barman, T. 2019, ApJ, 876, 69
Lothringer, J. D., Barman, T., & Koskinen, T. 2018, ApJ, 866, 27
McCullough, P. R., Crouzet, N., Deming, D., & Madhusudhan, N. 2014, ApJ, 791, 55
Mikal-Evans, T., Sing, D. K., Goyal, J. M., et al. 2019, MNRAS, 488, 2222
Oliphant, T. E. 2006, A Guide to NumPy, Vol. 1 (USA: Trelgol Publishing)
Parmentier, V., Line, M. R., Bean, J. L., et al. 2018, A&A, 617, A110
Pont, F., Knutson, H., Gilliland, R. L., Moutou, C., & Charbonneau, D. 2008, MNRAS, 385, 109
Pont, F., Sing, D. K., Gibson, N. P., et al. 2013, MNRAS, 432, 2917
Prez, F., & Granger, B. E. 2007, CSE, 9, 21
Rackham, B. V., Apai, D., & Giampapa, M. S. 2018, ApJ, 853, 122
Salz, M., Schneider, P. C., Fossati, L., et al. 2019, A&A, 623, A57
Schwenke, D. W. 1998, FaDi, 109, 321
Seidel, J. V., Ehrenreich, D., Wyttenbach, A., et al. 2019, A&A, 623, A166
Sing, D. K., Fortney, J. J., Nikolov, N., et al. 2016, Natur, 529, 59
Sing, D. K., Lavvas, P., Ballester, G. E., et al. 2019, AJ, 158, 91
Sing, D. K., Lecavelier des Etangs, A., Fortney, J. J., et al. 2013, MNRAS, 436, 2956
Sing, D. K., Vidal-Madjar, A., Désert, J.-M., Lecavelier des Etangs, A., & Ballester, G. 2008, ApJ, 686, 658
van der Walt, S., Colbert, S. C., & Varoquaux, G. 2011, CSE, 13, 22
Vidal-Madjar, A., Huitson, C. M., Bourrier, V., et al. 2013, A&A, 560, A54
Virtanen, P., Gommers, R., Oliphant, T. E., et al. 2020, NatMeth, 17, 261
von Essen, C., Mallonn, M., Welbanks, L., et al. 2019, A&A, 622, A71
Wakeford, H. R., Sing, D. K., Stevenson, K. B., et al. 2020, AJ, 159, 204
Yan, F., & Henning, T. 2018, NatAs, 2, 714
Zahnle, K., Marley, M. S., Freedman, R. S., Lodders, K., & Fortney, J. J. 2009, ApJ, 701, L20
Zhang, M., Chachan, Y., Kempton, E. M. R., & Knutson, H. A. 2019, PASP, 131, 034501